nanomaterials

MDPI

Article

Synthesis and Characterization of Highly Crystalline Bi-Functional Mn-Doped Zn_2SiO_4 Nanostructures by Low-Cost Sol–Gel Process

Dhiraj Kumar Bharti [1,2,3,4,*], **Rajni Verma** [5,*], **Sonam Rani** [4], **Daksh Agarwal** [6,7], **Sonali Mehra** [3,4], **Amit Kumar Gangwar** [8], **Bipin Kumar Gupta** [3,4], **Nidhi Singh** [4] and **Avanish Kumar Srivastava** [2,3,4]

1   Nanoscale Research Facility, Indian Institute of Technology Delhi, New Delhi 110016, India
2   CSIR—Advanced Materials and Processes Research Institute, Bhopal 462026, India
3   Academy of Scientific and Innovative Research (AcSIR), Ghaziabad 201002, India
4   CSIR—National Physical Laboratory, New Delhi 110012, India
5   School of Physics, The University of Melbourne, Parkville, VIC 3010, Australia
6   Department of Materials Science and Engineering, University of Pennsylvania, Philadelphia, PA 19104, USA
7   Lam Research Corporation, Fremont, CA 94538, USA
8   Teerthanker Mahaveer University, Moradabad 244001, India
*   Correspondence: dbharti5141@gmail.com (D.K.B.); rajni.verma@unimelb.edu.au (R.V.)

Abstract: Herein, we demonstrate a process for the synthesis of a highly crystalline bi-functional manganese (Mn)-doped zinc silicate (Zn_2SiO_4) nanostructures using a low-cost sol–gel route followed by solid state reaction method. Structural and morphological characterizations of Mn-doped Zn_2SiO_4 with variable doping concentration of 0.03, 0.05, 0.1, 0.2, 0.5, 1.0, and 2.0 wt% were investigated by using X-ray diffraction and high-resolution transmission electron microscopy (HR-TEM) techniques. HR-TEM-assisted elemental mapping of the as-grown sample was conducted to confirm the presence of Mn in Zn_2SiO_4. Photoluminescence (PL) spectra indicated that the Mn-doped Zn_2SiO_4 nanostructures exhibited strong green emission at 521 nm under 259 nm excitation wavelengths. It was observed that PL intensity increased with the increase of Mn-doping concentration in Zn_2SiO_4 nanostructures, with no change in emission peak position. Furthermore, magnetism in doped Zn_2SiO_4 nanostructures was probed by static DC magnetization measurement. The observed photoluminescence and magnetic properties in Mn-doped Zn_2SiO_4 nanostructures are discussed in terms of structural defect/lattice strain caused by Mn doping and the Jahn–Teller effect. These bi-functional properties of as-synthesized Zn_2SiO_4 nanostructures provide a new platform for their potential applications towards magneto-optical and spintronic and devices areas.

Keywords: Zn_2SiO_4; nanoparticles; transmission electron microscope; sol–gel; photoluminescence; lattice strain; nanomagnetism

1. Introduction

Multifunctional nanomaterials play an important role in different fields of applied sciences including semiconductor electronics, solar energy, memory devices, and optoelectronics devices for development of efficient nanosensors and nanosystems [1–6]. Therefore, tailoring of these nanomaterials for their desired properties is extremely important, especially for applications in advanced portable devices [7–12]. There are several nanomaterials which show tunability with size, shape, and properties with variation of doping concentration [9,13–16]. Zinc silicate especially (Zn_2SiO_4) is a promising candidate for applications in flat panel optical displays, UV detectors, gas sensors, adsorption of toxic ions from water, and thin film electro-luminescence devices applications [17–19]. Furthermore, Zn_2SiO_4 structures have received significant attention due to their unique wide range of multiple color luminescent properties, wide band gap (5.5 eV), and excellent chemical stability [20]. The willemite Zn_2SiO_4 host material is heavily used for applications in the field of phosphors for light emitting devices [21]. The Zn_2SiO_4 is a natural orthosilicate with

a phenacite-like structure in which Zn–O tetrahedral and Si–O tetrahedral share corners to form hollow 'tubes' parallel to [0001] planes; and it is a well-known host material for potential applications in the area of phosphors for optoelectronics and blue, green, and red color light emitting devices [1,3,20]. The incorporation of transition metal centers and rare earth ions (luminescence centers) in a Zn_2SiO_4 host lattice results in a various interesting luminescent property. Various methods such as vapor phase synthesis, high temperature solid-state reaction, and ball milling have been previously reported for synthesis of the Zn_2SiO_4 nanostructures. However, these reported methods require complicated procedure, huge thermal energy, high reaction temperature and time, and the synthesized materials exhibit irregular micro structure morphologies which is unsuitable for applications in devices where precise control over shapes and properties is required.

Recently, several new methods have been reported for the synthesis of Zn_2SiO_4 including sol–gel, polymer precursor, spray pyrolysis, and hydrothermal to get different luminescence emissions for various potential application [21–24]. R. Krsmanovic et al. prepared Sm- and Tb-doped Zn_2SiO_4 particle by sol–gel method to get reddish orange and pseudo white emissions [25]. H. Wang et al. and R. Pozas et al. prepared the Zn_2SiO_4 with Co dopant using hydrothermal method to obtain the blue pigments [26,27]. K Omri et al. reported the yellow phosphor of Mn-doped Zn_2SiO_4 using sol–gel method [28]. G. Gao et al. reported the Eu-doped Zn_2SiO_4 nanoparticles prepared by using solid state method to get red color emission [29]. Moreover, K. Omri et al., M. Hafeez et al., and W. Zheng et al. recently reported the diamagnetic and ferromagnetic properties from Mn-doped Zn_2SiO_4 nanostructures [30–32].

In the present investigations, we synthesized Mn-doped Zn_2SiO_4 nanostructures phosphors with various doping concentration using the cost effective and facile sol–gel method. Crystal structure, morphology, and photo luminescence properties of Mn-doped Zn_2SiO_4 nanostructures were studied. Effect of doping concentration of Mn in Zn_2SiO_4 on its structural, morphological, luminescence, and magnetic properties was also studied. Based on this, a correlation of lattice strain with observed magnetic properties and luminescence behavior is presented.

2. Materials and Methods

2.1. Materials

Manganese acetate ($Mn(CH_3COO)_2$; 99.999%), zinc chloride ($ZnCl_2$; 99.999%), tetraethyl orthosilicate ($Si(OC_2H_5)_4$; 99.999%), and ethanol (C_2H_5OH; 99.999%) were procured from Sigma Aldrich Chemicals Pvt Ltd., Delhi, India. Deionized water (DI) was obtained from a Direct-Q 3UV Millipore water purification system. Copper wires and silver paste were used to make the connection and contact, respectively.

2.2. Synthesis of Zn_2SiO_4 Nanoparticles

A flow chart for the preparation of Mn-doped Zn_2SiO_4 nanoparticles is shown in Figure 1. Mn-doped Zn_2SiO_4 nanoparticles were synthesized by sol–gel method under ambient atmosphere followed by thermal annealing. In the first step, 2.0433 mg of $ZnCl_2$ aqueous solution was prepared using 16 mL H_2O and 64 mL EtOH. Then, "x" amount (x = 0.03, 0.05, 0.1, 0.2, 0.5, 1.0, 2.0 wt%) of $Mn(CH_3COO)_2$ was dissolved into main solution. The prepared solution was mixed in a magnetic stirrer at 400 rpm at room temperature for 1 hr. Further, 2 mL of TEOS was slowly added drop by drop using micropipette while stirring after 1 h. Then, the solution was heated at 70 ^{0}C resulting, initially in the formation of a white gel and then into a powder when the gel was left overnight. This white powder was then calcined at 1000 °C in box furnace under natural atmospheric pressure for 6 h. Finally, the resultant white Zn_2SiO_4 nanoparticles was washed with distilled water and collected for characterization.
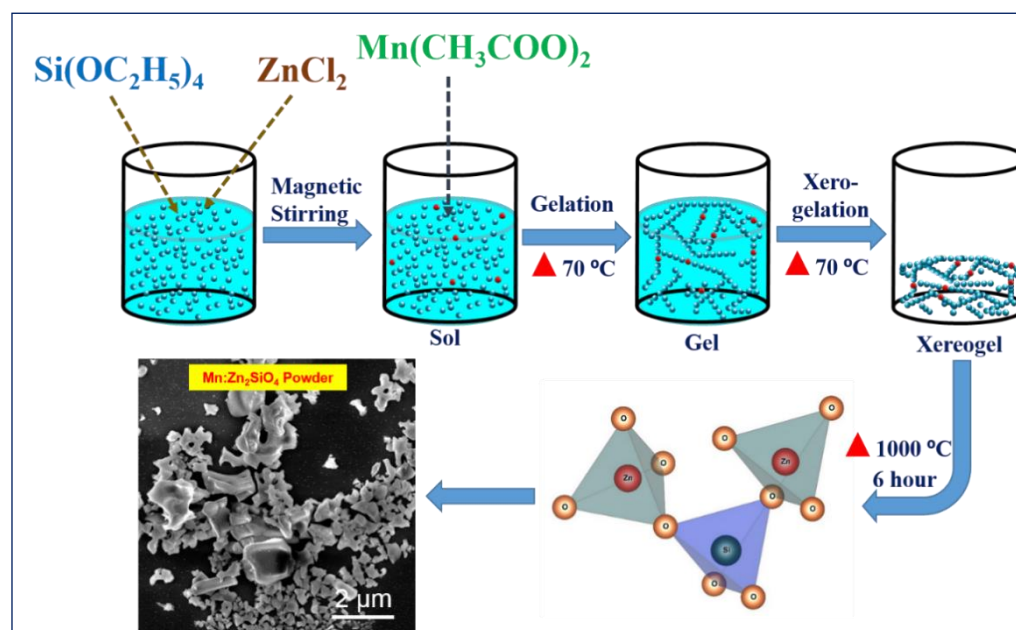
Figure 1. Schematic diagram of sol–gel method for the synthesis of Mn-doped Zn_2SiO_4 green phosphor nanoparticles. Red triangle corresponds to heating.
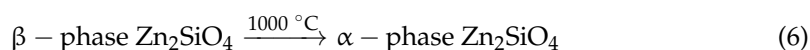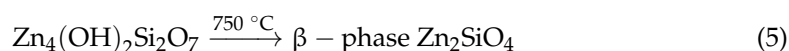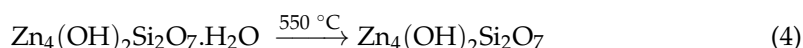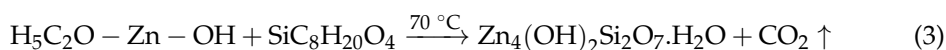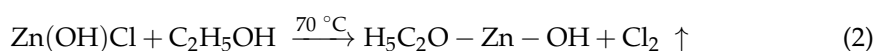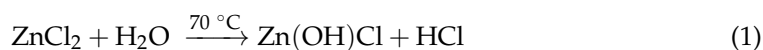
2.3. Measurement and Characterizations

The structural properties of the prepared samples were measured by X-ray diffraction (XRD) technique using a Rigaku (ultima IV model, Japan) benchtop X-ray diffractometer equipped with a monochromatic Cu-Kα radiation (λ = 1.541 Å) X-ray source. The morphology of the samples was analyzed by high resolution transmission electron microscopy (HR-TEM) JEM 2100F operating at 200 keV and the attached GATAN (Version: GMS 2.32) digital-micrograph software. Elemental mapping was performed using Oxford attachment in HRTEM. The room temperature photoluminescence (PL) investigation was performed using a Perkin Elmer LS-55 fluorescence spectrophotometer with a Xenon (Xe) lamp as the source of excitation. The magnetic properties at room temperature were examined by a SQUID magnetometer (MPMS7 Tesla, Quantum Design, San Diego, CA, USA) in the field range $\pm$ 2T with a step size of 400 Oe and a field scan rate of 100 Oe per minute.

3. Results and Discussion

3.1. Formation of α-Phase Zn_2SiO_4

The chemical reaction process and crystal growth mechanism for formation of α-phase Zn_2SiO_4 nanostructures can be explained by the following chemical reaction steps:

$$ZnCl_2 + H_2O \xrightarrow{70\,^{\circ}C} Zn(OH)Cl + HCl \tag{1}$$

$$Zn(OH)Cl + C_2H_5OH \xrightarrow{70\,^{\circ}C} H_5C_2O - Zn - OH + Cl_2 \uparrow \tag{2}$$

$$H_5C_2O - Zn - OH + SiC_8H_{20}O_4 \xrightarrow{70\,^{\circ}C} Zn_4(OH)_2Si_2O_7.H_2O + CO_2 \uparrow \tag{3}$$

$$Zn_4(OH)_2Si_2O_7.H_2O \xrightarrow{550\,^{\circ}C} Zn_4(OH)_2Si_2O_7 \tag{4}$$

$$Zn_4(OH)_2Si_2O_7 \xrightarrow{750\,^{\circ}C} \beta - phase\ Zn_2SiO_4 \tag{5}$$

$$\beta - phase\ Zn_2SiO_4 \xrightarrow{1000\,^{\circ}C} \alpha - phase\ Zn_2SiO_4 \tag{6}$$

The reaction mechanism leading to the formation of zinc silicate can be summarized in the following steps. In the first step, $ZnCl_2$ reacts with H_2O and C_2H_5OH at 70 °C and is transformed into Zn (OH)Cl. Then, this Zn(OH)Cl reacts with TEOS, and hydrated

hemimorphite leading to formation of $Zn_4(OH)_2Si_2O_7.H_2O$ powder. This powder, when annealed at ~550 °C forms dehydrated hemimorphite $Zn_4(OH)_2Si_2O_7$. Dehydrated hemimorphite $Zn_4(OH)_2Si_2O_7$ is transformed into β-phase $ZnSi_2O_7$ by annealing at ~750 °C and into α-phase Zn_2SiO_4 by annealing at 1000 °C.

3.2. Structural Analysis

The X-ray diffraction (XRD) pattern of the annealed Zn_2SiO_4 nanostructures collected at room temperature is shown in Figure 2. All diffraction peaks in the pattern can be indexed to the crystalline willemite (α-Zn_2SiO_4, JCPDS card 37-1485) structure of rhombohedral system with lattice parameters a = b = 13.938 Å and c = 9.31 Å, α = β = 90°, γ = 120° revealing the crystallinity of the samples [33].
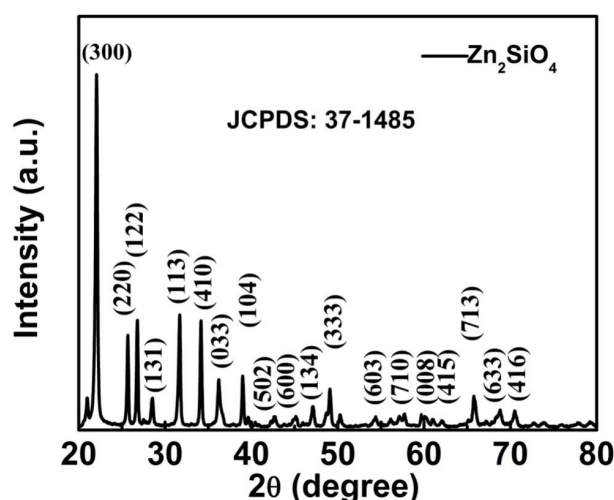

Figure 2. The XRD pattern of Zn_2SiO_4 nanostructures annealed at 1000 °C.

The average crystallite size of the as grown samples was calculated using the Williamson and Hall method which is a combination of the Scherrer's equation for size broadening and the Stokes and Wilson expression for strain broadening [34–37].

$$\beta \cos\theta_B = \frac{k\lambda}{D} + 4\eta \sin\theta_B \tag{7}$$

where β is the full width at half maximum of diffraction peak, η is the strain in the crystallites, and D is the crystallites size [38–40]. The constant k is typically close to unity and ranges from 0.8 to 1.39. To calculate the strain and crystallite size, a graph was plotted in between $\beta \cos\theta_B$ and $\sin\theta_B$. The strain (η) was then extracted from the slope and the crystallite size was determined from the y-intercept. The average crystallite size of the undoped Zn_2SiO_4 nanostructures was found to be 28 nm.

The XRD patterns of Zn_2SiO_4 samples doped with various doping concentration of Mn are shown in Figure 3a. The result shows that the diffraction peaks of nanostructures shifted towards lower angle with an increase in Mn concentration. This shift in the diffraction peak can be attributed to lattice expansion as a result of induced strain from Mn doping. The likely position of Mn substitution in Zn_2SiO_4 lattice is shown in the Figure 3b and it is proposed that Mn^{2+} occupies the Zn^{2+} position. Furthermore, a close view of unit cell can be easily seen from right inset (top and bottom) of Figure 3b.

The different doping concentration of Mn substitution in Zn_2SiO_4 lattice and lattice expansion can be easily understood by strain effect as shown in Figure S1. N. Tripathi et al., D.H. Hwang et al., and M.S. Kwon et al. observed the same trend where strain induced effect of Mn in the Zn_2SiO_4 nanocrystals enhances the green emission efficiency with short decay time [41–43]. The result clearly indicates that the different doping concentration significantly affects the packing of unit cell such as dislocation of host Zn site. Further, the dislocation is confirmed by a Williamson and Hall in the form of strain developed

in the lattice which results in slight angle shifts in XRD spectra as shown in Figure 3a. Moreover, depending on different θ positions, the separation of size and strain broadening analysis is done using Williamson and Hall method. Crystal imperfections and distortion of strain-induced peak broadening can be related by the well-known Williamson and Hall method shown in Figure S1.
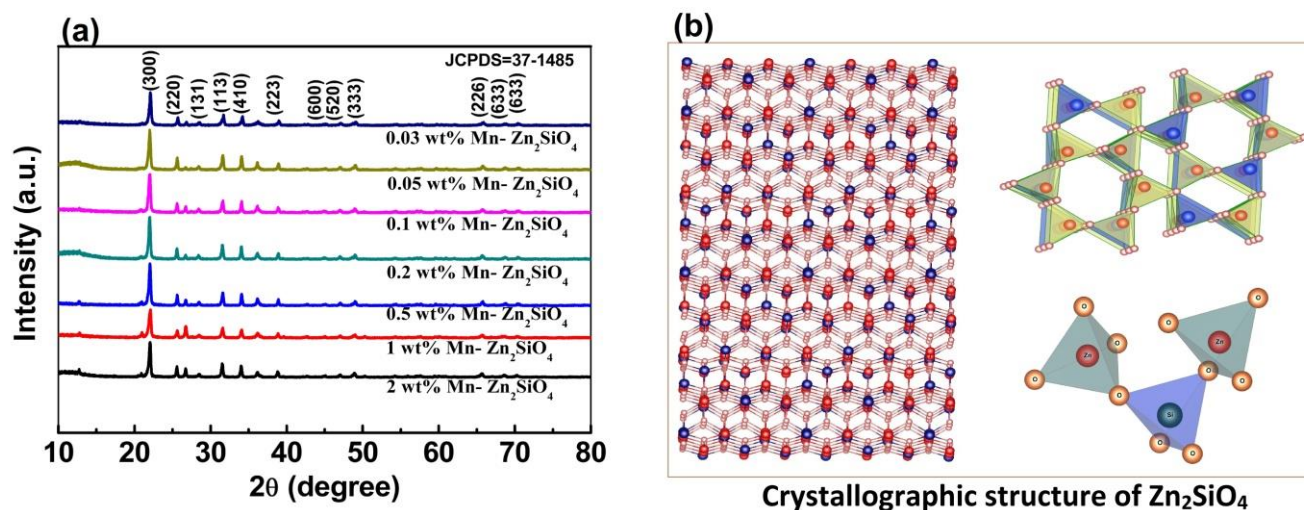

Figure 3. (**a**) XRD patterns of Zn_2SiO_4 with different Mn doping concentrations ranging from 0.03 wt% to 2 wt%. (**b**) Unit cell of Zn_2SiO_4 and in case of Mn doping, Mn goes to Zn site (Zn^{2+}: Red; Si^{4+}: Blue; O^{2-}:Orange).

Figure 4 shows the calculated strain and crystalline size of Zn_2SiO_4 as a function of % of Mn doping. It is clearly observed that the strain increases with an increase in Mn doping in the host lattice. The obtained results also indicate that crystallite size increases due to differences in ionic radius between Mn^{2+} and Zn^{2+}. (The ionic radii of Zn and Mn are 0.083 and 0.091 nm, respectively).
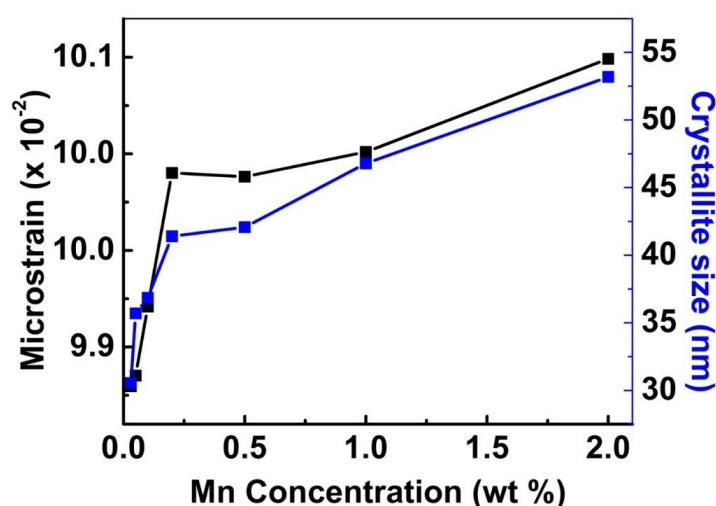

Figure 4. Comparative strain (black square) and crystallite size (blue square) of Zn_2SiO_4 as a function of Mn doping in Zn_2SiO_4 host lattice.

3.3. Morphology Analysis

The morphology and microstructure of the as-synthesized Zn_2SiO_4 nanostructure was analyzed by high-resolution transmission electron microscope (HR-TEM). Figure 5a shows the nanorod-like morphology of 0.2 wt% Mn-doped Zn_2SiO_4. The estimation of the dimension of individual nanorods is presented in the inset of Figure 5a. Figure 5b

shows the magnified view of nanorod-like morphology of the individual rod with 620 nm length and 300 nm width. Its selected area electron diffraction (SAED) pattern recorded without sample tilting is shown in the inset of Figure 5b. The SAED result reveals that the nanorod is crystalline in nature. The HR-TEM image of the nanorod in Figure 5c shows regular lattice fringes with d-spacing of 0.26 nm, which is in agreement with the inter planar spacing of (300) plane in XRD pattern. Figure 5d shows the magnified view of nanoflake-like morphology of individual rod with length of 970 nm and width of 370 nm. The inset in Figure 5d shows the clear lattice fringe of nanorods which corresponds to 113 plane.
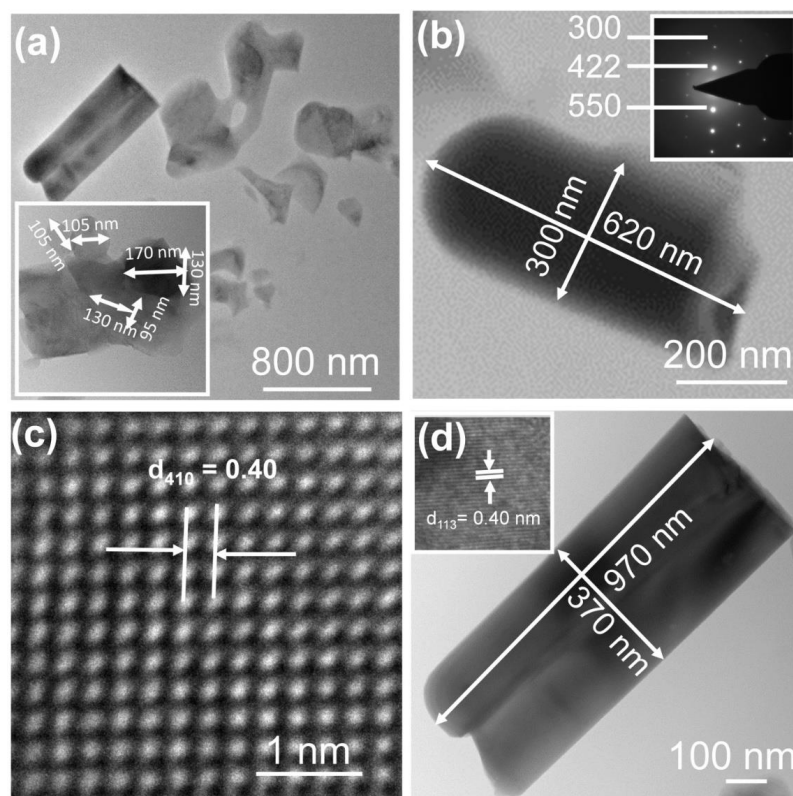

Figure 5. (**a**) Nanorod-like morphology of a 0.2 wt% Mn-doped Zn_2SiO_4. (**b**) Magnified view of nanorod-like morphology of individual rod with length 620 nm and width 300 nm. Inset shows the SAED result. (**c**) The HR-TEM image of nanorod. (**d**) HRTEM image of nanoflake-like morphology of individual rod of length 970 nm and width 370 nm. Inset shows the lattice fringe of nanorods corresponding to 113 plane.

The elemental mapping of the as-synthesized 0.2 wt% Mn-doped Zn_2SiO_4 samples was done by energy dispersive spectroscopy (EDS) added to the HR-TEM instrument. The spectra obtained from the EDS mapping are shown in Figure 6 which confirms the Mn doping in Zn_2SiO_4 lattice. The elements present in two different regions of the sample (Figure 6a) are shown in the Figure 6b–e for first region and 6f–i for the second region highlighting the elemental homogeneity of the grown samples. The elemental maps micrographs of Mn, Zn, Si, and O show a uniform distribution over the entire morphology of Mn-doped Zn_2SiO_4 nanostructure in both the regions. A quantitative analysis carried out to estimate the weight and atomic percentage of samples is shown in the Figure 6j. The observed spectra show that peak detected at 1.740 eV, 0.525 eV, 8.639 eV corresponds to the $K\alpha_1$ of Si, $K\alpha_1$ of O, and $K\alpha_1$ of Zn, respectively. Further, the peaks detected at 9.572 eV and 1.012 eV correspond to the $K\beta_1$ of Zn, and $K\alpha_1$, $k\beta_2$ of Zn, respectively. The peak observed at 5.899 eV correspond to the $K\alpha_1$ of Mn and peak, 6.491 eV, 0.636 eV corresponds to the $K\beta_1$ of Mn and $L\alpha_1$ and $L\alpha_2$ of Mn, respectively [30,44].
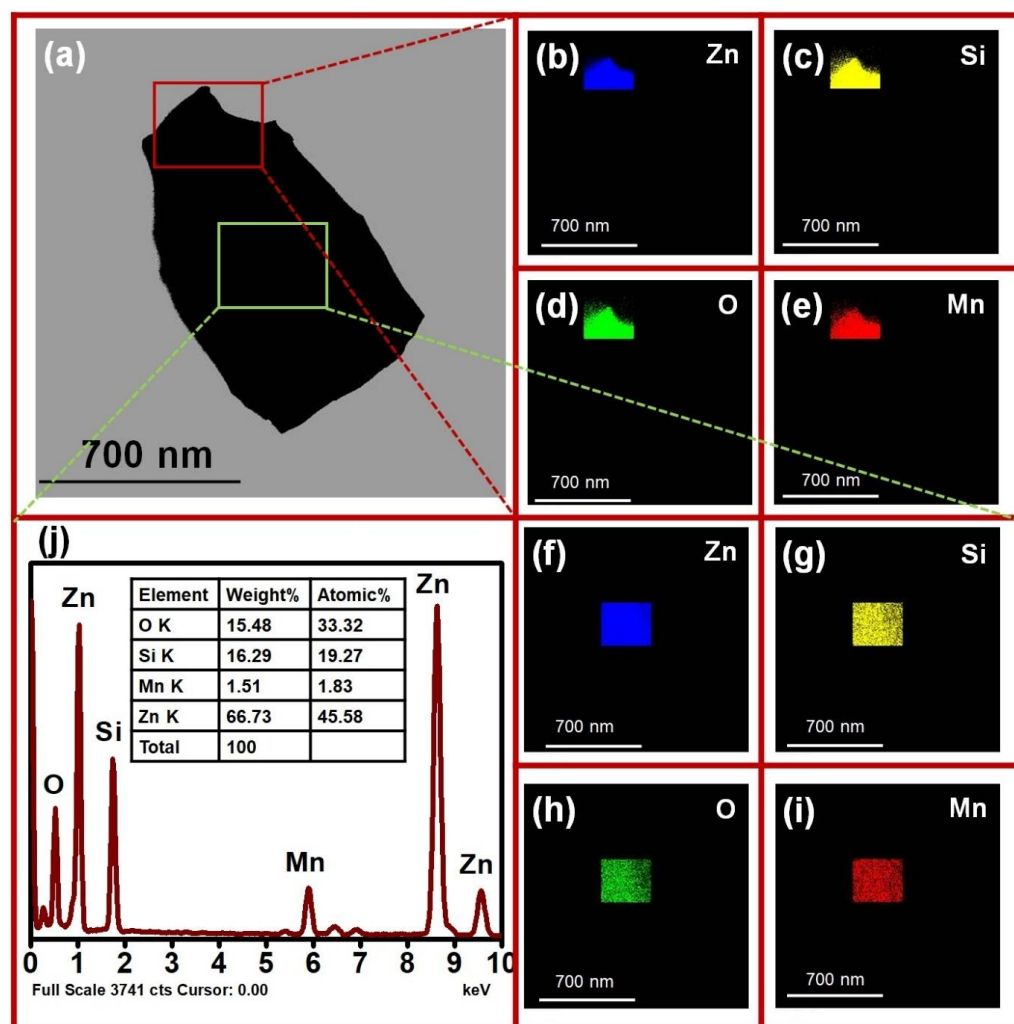
**Figure 6.** (**b–i**) show the spectra obtained from the EDS mapping of (**a**) which confirmed the Mn doping in Zn_2SiO_4 lattice. (**j**) shows the quantitative analysis was also carried out to estimate the weight and atomic percentage of samples and EDS spectra.

3.4. Photoluminescence Analysis

Figure 7a shows the photoluminescence (PL) spectra of Mn-doped Zn_2SiO_4 measured with an excitation wavelength of 259 nm at room temperature (Figure 7b). The emission spectra of the samples show broad green emission centered at 521 nm which arises due to Mn^{2+} ion transitions. The green emission from the sample can be understood in terms of various transition states of Mn element. The green PL emission results transition from the $^4T_1(^4G)$ excited state to the $^6A_1$ (^6S) ground state in 3D orbital electrons of the Mn^{2+} ion [45]. The variation in the PL intensity is due to the size variation and defect level introduced from the doping. It is noted that the nanostructure has large surface area, which significantly impairs the PL intensity by introducing a correspondingly large number of defects. The transition of free electrons in the conduction band by the charge transfer transition of Mn is as described below

$$Mn^{2+}(3d^5) \rightarrow Mn^{3+} + (3d^4) + Eg_{CB} \tag{8}$$
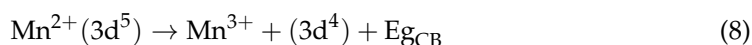
These excited free electrons further relax from the conduction band to the $^4T_1(^4G)$ lowest excitation energy level of the Mn^{2+} ion via non-radiative transitions, followed by a radiative transition from the $^4T^1(^4G)$ level to the $^6A_1(^6S)$ ground state or valance state which results in the green PL emission peak centered at 521 nm. A schematic image of the corresponding transition is shown in the Figure 7b. Changing the doping % of Mn^{2+} resulted in only a very small shift in peak position. However, the PL intensity shows

nonlinear trend with doping concentration. For better understanding, the PL peak intensity as a function of x at 521 nm was also plotted along with the FWHM as a function of x and is shown in Figure S2. It is clearly observed that the PL intensity first increases with doping concentration with a maxima at 0.2 wt% and then decreases with a further increase in doping. As Mn concentration increases from 0.03 wt % to 0.2 wt%, stress in the crystal lattice also increases as discussed in the XRD section and also shown in Table S1. The decrease of intensity with higher concentration of Mn doping is due to activator concentration quenching and the decrease in the inter-ionic distance between two adjacent Mn^{2+} ion pairs. This reduction of inter-ionic distance between the Mn^{2+} ion pairs leads to exchange of excited free electron migration from one Mn^{2+} ion to another, which causes non-radiative transitions and reduces the emission efficiency and the demonstration at 0.4 wt% Mn doped Zn_2SiO_4 is shown in Video V1 [46].
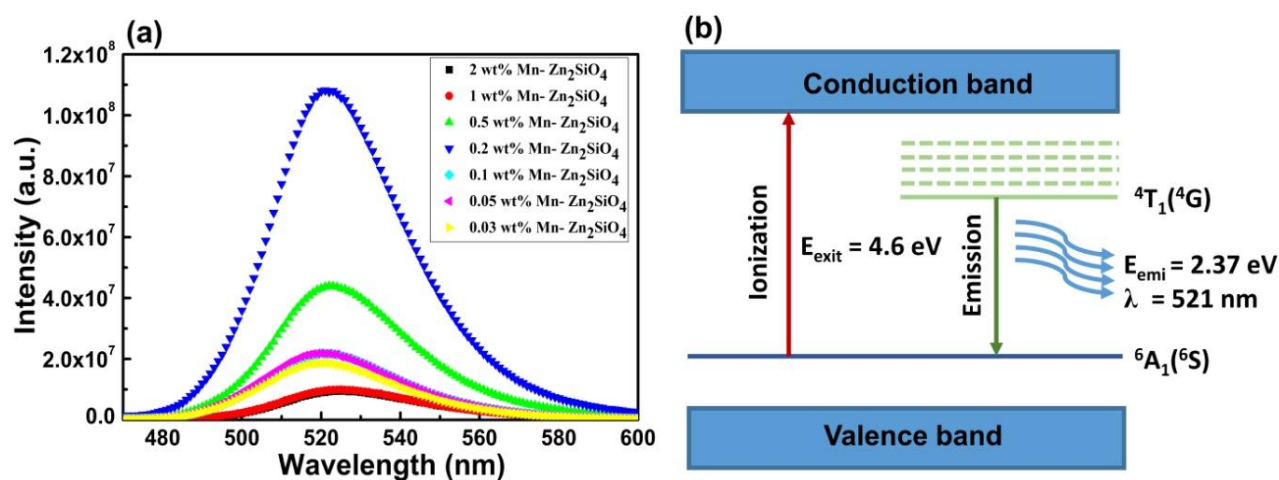

Figure 7. (**a**) shows the broad PL emission band centered at 521 nm of Zn_2SiO_4 doped at different concentrations of Mn at an excitation wavelength of 259 nm at room temperature. (**b**) shows a schematic image of shows the green PL emission peak centered at 521 nm transition from the $^4T_{1n}(^4G)$ excited state to the $^6A_1$ (^6S) ground state.

3.5. Magnetic Analysis

The M-H plot of Mn-doped Zn_2SiO_4 nanorods at room temperature is shown in Figure 8a. It is observed that the value of magnetization increased with increase in the Mn doping concentration, which may be due to the increased amount of impurity in the host lattice of Zn_2SiO_4 [47,48]. It was observed in the present study that pristine Zn_2SiO_4 exhibits only diamagnetic behavior at room temperature. Further, observed remanence and coercivity for higher Mn content indicates nucleation of ferromagnetic characteristic, whereas diamagnetic behavior was found to be still prevailing for lower Mn^{2+} content. The M-H loops of all the samples were plotted after substituting the diamagnetic contribution of each of the sample [36,37,49]. Magnetization of Zn_2SiO_4 with increased Mn doping can be explained in terms of the Jahn–Teller effect which relates the suppressing the spiral spin structure of Zn_2SiO_4 by the incorporation of Mn at Zinc sites [30,31]. It is also proposed that Mn cations presented in the Zn_2SiO_4 are in mixed valence states of 2+, 3+, and 4+ which could support ferromagnetic coupling through Zener double exchange interaction. In low concentration, the Jahn–Teller effect would be expected to cause a reduction in the tendency toward ferromagnetism since it leads to a splitting of the states. The splitting will reduce the interactions between Mn pairs since hopping requires an extra energy [9,14,34,35,50]. On the other hand, the interaction between Mn–Mn pairs at realistic distances is sufficiently large that it dominates over the Jahn–Teller effect. The interactions between Mn atoms is not greatly affected by lattice relaxations and there is always a clear tendency for ferromagnetic alignment of Mn pairs as evidenced in the present study for higher Mn concentrations.

Figure 8b shows value of magnetization with increase in Mn doping wt% concentration into Zn_2SiO_4 host lattice.
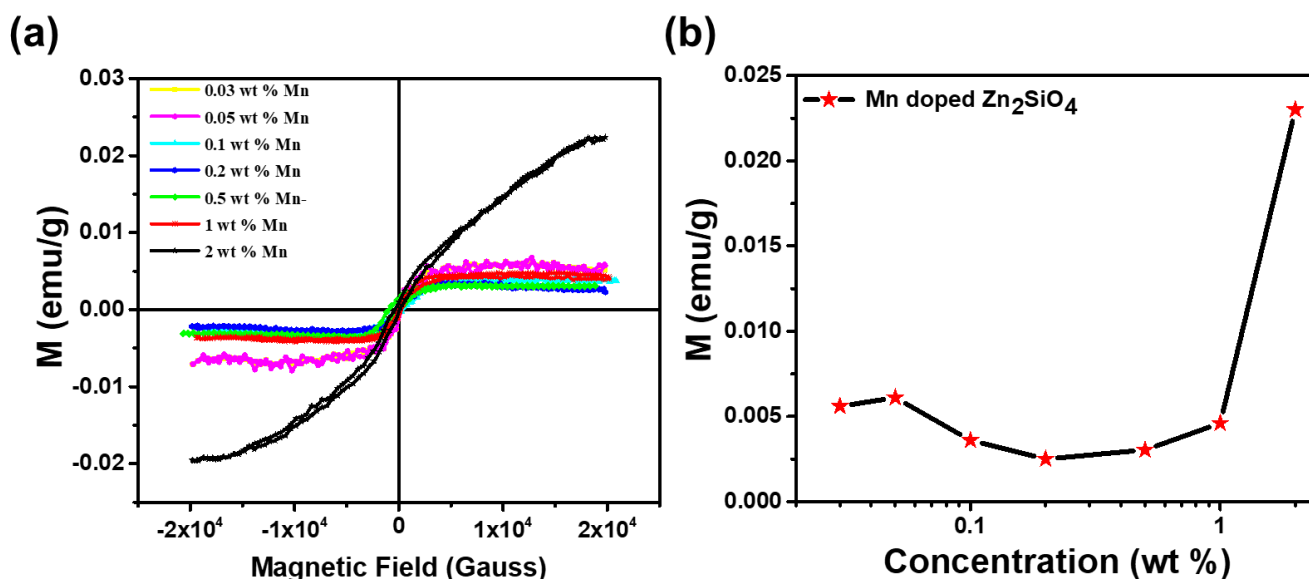

Figure 8. (**a**) M-H plot of Mn-doped Zn_2SiO_4 nanoparticles at room temperature. (**b**) Saturation magnetization as a function of Mn wt% in Zn_2SiO_4 host lattice.

4. Conclusions

We successfully synthesized highly crystalline bi-functional Mn-doped Zn_2SiO_4 nanostructures with various doping concentration using a low-cost sol–gel process. The X-ray diffraction results confirmed the rhombohedral phase of Mn-doped Zn_2SiO_4 nanostructure. The HR-TEM results confirm the nanorod-like morphology. The PL results show the strong green emission peak centered at 521 nm under 259 nm excitation wavelength. The optimization for highest photoluminescence intensity was achieved by varying different concentrations of Mn-doping in Zn_2SiO_4 lattice. We observed that 0.2 wt% Mn doping in Zn_2SiO_4 nanostructure showed the highest PL intensity. Magnetic studies confirmed the magnetic nature of Mn-doped Zn_2SiO_4 nanostructures and magnetization increased with increase of Mn concentration. Thus, the bi-functional behavior of Mn-doped Zn_2SiO_4 nanostructures offers a new avenue to further exploit its potential application in magneto-optical devices.

Conflicts of Interest: The authors declare no conflict of interest.

References

1. Bharti, D.K.; Gupta, M.K.; Kumar, R.; Sathish, N.; Srivastava, A.K. Non-centrosymmetric zinc silicate-graphene based transparent flexible piezoelectric nanogenerator. *Nano Energy* **2020**, *73*, 104821. [CrossRef]
2. Bharti, D.K.; Gupta, M.K.; Srivastava, A.K. Giant dielectric constant and band gap reduction in hydrothermal grown highly crystalline zinc silicate nanorods. *Mater. Lett.* **2018**, *232*, 66–69. [CrossRef]
3. Bharti, D.K.; Veeralingam, S.; Badhulika, S. An ultra high performance, lead-free Bi_2WO_6:P(VDF-TrFE)-based triboelectric nanogenerator for self-powered sensors and smart electronic applications. *Mater. Horiz.* **2022**, *9*, 663–674. [CrossRef] [PubMed]
4. Pathak, S.; Jain, K.; Kumar, V.; Pant, R.P. Magnetic Fluid Based High Precision Temperature Sensor. *IEEE Sens. J.* **2017**, *17*, 2670–2675. [CrossRef]
5. Pathak, S.; Zhang, R.; Gayen, B.; Kumar, V.; Zhang, H.; Pant, R.P.; Wang, X. Ultra-low friction self-levitating nanomagnetic fluid bearing for highly efficient wind energy harvesting. *Sustain. Energy Technol. Assess.* **2022**, *52*, 102024. [CrossRef]
6. Verma, R.; Pathak, S.; Srivastava, A.K.; Prawer, S.; Tomljenovic-Hanic, S. ZnO nanomaterials: Green synthesis, toxicity evaluation and new insights in biomedical applications. *J. Alloys Compd.* **2021**, *876*, 160175. [CrossRef]
7. Verma, R.; Gangwar, J.; Srivastava, A.K. Multiphase TiO_2 nanostructures: A review of efficient synthesis, growth mechanism, probing capabilities, and applications in bio-safety and health. *RSC Adv.* **2017**, *7*, 44199–44224. [CrossRef]
8. Kumar, M.; Rani, S.; Kumar, A.; Tawale, J.; Srivastava, R.; Singh, B.P.; Pathak, S.; Wang, X.; Singh, V.N. Broadband (NIR-Vis-UV) photoresponse of annealed SnSe films and effective oxidation passivation using Si protective layer. *Mater. Res. Bull.* **2022**, *153*, 111913. [CrossRef]
9. Gbadamasi, S.; Mohiuddin, M.; Krishnamurthi, V.; Verma, R.; Khan, M.W.; Pathak, S.; Kalantar-Zadeh, K.; Mahmood, N. Interface chemistry of two-dimensional heterostructures—Fundamentals to applications. *Chem. Soc. Rev.* **2021**, *50*, 4684–4729. [CrossRef]
10. Verma, R.; Pathak, S.; Dey, K.K.; Sikarwar, S.; Yadav, B.C.; Srivastava, A.K. Facile synthesized zinc oxide nanorod film humidity sensor based on variation in optical transmissivity. *Nanoscale Adv.* **2022**, *4*, 2902–2912. [CrossRef]
11. Goswami, L.; Aggarwal, N.; Verma, R.; Bishnoi, S.; Husale, S.; Pandey, R.; Gupta, G. Graphene quantum dots sensitized ZnO-Nanorods/GaN-Nanotowers heterostructure based high performance UV Photodetector. *ACS Appl. Mater. Interfaces* **2020**, *12*, 47038–47047. [CrossRef] [PubMed]
12. Goswami, L.; Aggarwal, N.; Singh, M.; Verma, R.; Vashishtha, P.; Jain, S.K.; Tawale, J.; Pandey, R.; Gupta, G. GaN Nanotowers Grown on Si (111) and Functionalized with Au Nanoparticles and ZnO Nanorods for Highly Responsive UV Photodetectors. *ACS Appl. Nano Mater.* **2020**, *3*, 8104–8116. [CrossRef]
13. Singh, D.; Kundu, V.S.; Dhiman, R.L.; Gangwar, J. Structural and morphological study of zinc doped tin oxide nanoparticles synthesized via sol-gel technique. *AIP Conf. Proc.* **2018**, *2006*, 030017.
14. Kumar, P.; Pathak, S.; Singh, A.; Jain, K.; Khanduri, H.; Wang, L.; Kim, S.-K.; Pant, R.P. Observation of intrinsic fluorescence in cobalt ferrite magnetic nanoparticles by Mn^{2+} substitution and tuning the spin dynamics by cation distribution. *J. Mater. Chem. C* **2022**, *10*, 12652–12679. [CrossRef]
15. Pathak, S.; Zhang, R.; Bun, K.; Zhang, H.; Gayen, B.; Wang, X. Development of a novel wind to electrical energy converter of passive ferrofluid levitation through its parameter modelling and optimization. *Sustain. Energy Technol. Assess.* **2021**, *48*, 101641. [CrossRef]
16. Bakshi, P.; Pappu, A.; Kumar Bharti, D. Transformation of flue gas desulfurization (FGD) gypsum to β-CaSO$_4\cdot$0.5H$_2$O whiskers using facile water treatment. *Mater. Lett.* **2021**, *308*, 131177. [CrossRef]
17. Dai, P.; Xu, Z.; Yu, X.; Wang, Y.; Zhang, L.; Li, G.; Sun, Z.; Liu, X.; Wu, M. Mesoporous hollow Zn_2SiO_4:Mn^{2+} nanospheres: The study of photoluminescence and adsorption properties. *Mater. Res. Bull.* **2015**, *61*, 76–82. [CrossRef]
18. Basavaraj, R.B.; Nagabhushana, H.; Daruka Prasad, B.; Sharma, S.C.; Prashantha, S.C.; Nagabhushana, B.M. A single host white light emitting Zn_2SiO_4:Re^{3+} (Eu, Dy, Sm) phosphor for LED applications. *Opt.—Int. J. Light Electron Opt.* **2015**, *126*, 1745–1756. [CrossRef]
19. Qu, J.; Cao, C.-Y.; Hong, Y.-L.; Chen, C.-Q.; Zhu, P.-P.; Song, W.-G.; Wu, Z.-Y. New hierarchical zinc silicate nanostructures and their application in lead ion adsorption. *J. Mater. Chem.* **2012**, *22*, 3562–3567. [CrossRef]
20. Zhang, S.; Lu, M.; Li, Y.; Sun, F.; Yang, J.; Wang, S. Synthesis and electrochemical properties of Zn_2SiO_4 nano/mesorods. *Mater. Lett.* **2013**, *100*, 89–92. [CrossRef]
21. El Ghoul, J.; Omri, K.; El Mir, L.; Barthou, C.; Alaya, S. Sol-gel synthesis and luminescent properties of SiO_2/Zn_2SiO_4 and SiO_2/Zn_2SiO_4:V composite materials. *J. Lumin.* **2012**, *132*, 2288–2292. [CrossRef]
22. Su, K.; Tilley, T.D.; Sailor, M.J. Molecular and Polymer Precursor Routes to Manganese-Doped Zinc Orthosilicate Phosphors. *J. Am. Chem. Soc.* **1996**, *118*, 3459–3468. [CrossRef]
23. Li, Q.H.; Komarneni, S.; Roy, R. Control of morphology of Zn_2SiO_4 by hydrothermal preparation. *J. Mater. Sci.* **1995**, *30*, 2358–2363. [CrossRef]

24. Kang, Y.C.; Park, S.B. Zn$_2$SiO$_4$:Mn phosphor particles prepared by spray pyrolysis using a filter expansion aerosol generator. *Mater. Res. Bull.* **2000**, *35*, 1143–1151. [CrossRef]

25. Krsmanović Whiffen, R.; Antić, Ž.; Marinović-Cincović, M.; Dramicanin, M. Samarium and terbium doped Zn$_2$SiO$_4$ phosphors obtained by polymer supported sol-gel synthesis. *J. Optoelectron. Adv. Mater.* **2009**, *1*, 37–41.

26. Wang, H.; Ma, Y.; Yi, G.; Chen, D. Synthesis of Mn-doped Zn$_2$SiO$_4$ rodlike nanoparticles through hydrothermal method. *Mater. Chem. Phys.* **2003**, *82*, 414–418. [CrossRef]

27. Pozas, R.; Orera, V.M.; Ocaña, M. Hydrothermal synthesis of Co-doped willemite powders with controlled particle size and shape. *J. Eur. Ceram. Soc.* **2005**, *25*, 3165–3172. [CrossRef]

28. Omri, K.; Lassaad, E.M.; Dahman, H.; Barthou, C. Synthesis and Luminescence Properties of Yellow-emitting SiO$_2$/Zn$_2$SiO$_4$:Mn Nanocomposite. *Sens. Tranducers* **2014**, *27*, 295–298.

29. Gao, G.; Reibstein, S.; Peng, M.; Wondraczek, L. Tunable dual-mode photoluminescence from nanocrystalline Eu-doped Li$_2$ZnSiO$_4$ glass ceramic phosphors. *J. Mater. Chem.* **2011**, *21*, 3156–3161. [CrossRef]

30. Omri, K.; Alyamani, A.; Mir, L.E. Photoluminescence and cathodoluminescence of Mn doped zinc silicate nanophosphors for green and yellow field emissions displays. *Appl. Phys. A* **2018**, *124*, 215–221. [CrossRef]

31. Hafeez, M.; Ali, A.; Manzoor, S.; Bhatti, A.S. Anomalous optical and magnetic behavior of multi-phase Mn doped Zn$_2$SiO$_4$ nanowires: A new class of dilute magnetic semiconductors. *Nanoscale* **2014**, *6*, 14845–14855. [CrossRef]

32. Wan, J.; Wang, Z.; Chen, X.; Mu, L.; Yu, W.; Qian, Y. Controlled synthesis and relationship between luminescent properties and shape/crystal structure of Zn$_2$SiO$_4$:Mn^{2+} phosphor. *J. Lumin.* **2006**, *121*, 32–38. [CrossRef]

33. El Ghoul, J.; Barthou, C.; Saadoun, M.; El Mir, L. Synthesis and optical characterization of SiO$_2$/Zn$_2$SiO$_4$:Mn nanocomposite. *Phys. B Condens. Matter* **2010**, *405*, 597–601. [CrossRef]

34. Kumar, P.; Khanduri, H.; Pathak, S.; Singh, A.; Basheed, G.A.; Pant, R.P. Temperature selectivity for single phase hydrothermal synthesis of PEG-400 coated magnetite nanoparticles. *Dalton Trans.* **2020**, *49*, 8672–8683. [CrossRef] [PubMed]

35. Kumar, P.; Pathak, S.; Singh, A.; Khanduri, H.; Basheed, G.A.; Wang, L.; Pant, R.P. Microwave spin resonance investigation on the effect of the post-processing annealing of CoFe$_2$O$_4$ nanoparticles. *Nanoscale Adv.* **2020**, *2*, 1939–1948. [CrossRef]

36. Pathak, S.; Verma, R.; Kumar, P.; Singh, A.; Singhal, S.; Sharma, P.; Jain, K.; Pant, R.P.; Wang, X. Facile Synthesis, Static, and Dynamic Magnetic Characteristics of Varying Size Double-Surfactant-Coated Mesoscopic Magnetic Nanoparticles Dispersed Stable Aqueous Magnetic Fluids. *Nanomaterials* **2021**, *11*, 3009. [CrossRef] [PubMed]

37. Pathak, S.; Verma, R.; Singhal, S.; Chaturvedi, R.; Kumar, P.; Sharma, P.; Pant, R.P.; Wang, X. Spin dynamics investigations of multifunctional ambient scalable Fe$_3$O$_4$ surface decorated ZnO magnetic nanocomposite using FMR. *Sci. Rep.* **2021**, *11*, 3799. [CrossRef]

38. Williamson, G.K.; Hall, W.H. X-ray line broadening from filed aluminium and wolfram. *Acta Metall.* **1953**, *1*, 22–31. [CrossRef]

39. Basheed, G.A.; Jain, K.; Pathak, S.; Pant, R.P. Dipolar Interaction and Magneto-Viscoelasticity in Nanomagnetic Fluid. *J. Nanosci. Nanotechnol.* **2018**, *18*, 2746–2751.

40. Jain, K.; Pathak, S.; Pant, R.P. Enhanced magnetic properties in ordered oriented ferrofibres. *RSC Adv.* **2016**, *6*, 70943–70946. [CrossRef]

41. Tripathi, N.; Akai, T. Structural designing of Zn$_2$SiO$_4$:Mn nanocrystals by co-doping of alkali metal ions in mesoporous silica channels for enhanced emission efficiency with short decay time. *RSC Adv.* **2021**, *11*, 36348–36353. [CrossRef] [PubMed]

42. Hwang, D.H.; Han, K.S.; Lee, B.H. Synthesis and Formation Mechanism of Mn-Doped Zn$_2$SiO$_4$ Brown Pigment. *Mater. Sci. Forum* **2011**, *695*, 295–298. [CrossRef]

43. Kwon, M.S.; Kim, C.J.; Park, H.L.; Kim, T.W.; Lee, H.S. Sol–gel synthesis and green luminescence of nanocrystalline Zn$_2$SiO$_4$:Mn phosphor. *J. Mater. Sci.* **2005**, *40*, 4089–4091. [CrossRef]

44. Hu, T.; Lin, H.; Xu, J.; Wang, B.; Wang, J.; Wang, Y. Color-tunable persistent luminescence in oxyfluoride glass and glass ceramic containing Mn^{2+}:α-Zn$_2$SiO$_4$ nanocrystals. *J. Mater. Chem. C* **2017**, *5*, 1479–1487. [CrossRef]

45. Yoon, K.H.; Kim, J.H. Optical Properties and Photoluminescent Characteristics of Manganese-doped Zinc Silicate Thin Films. *J. Korean Phys. Soc.* **2011**, *6*, 1668–1671. [CrossRef]

46. Lu, Q.; Wang, P.; Li, J. Structure and luminescence properties of Mn-doped Zn$_2$SiO$_4$ prepared with extracted mesoporous silica. *Mater. Res. Bull.* **2011**, *46*, 791–795. [CrossRef]

47. Omri, K.; Lemine, O.M.; El Mir, L. Mn doped zinc silicate nanophosphor with bifunctionality of green-yellow emission and magnetic properties. *Ceram. Int.* **2017**, *43*, 6585–6591. [CrossRef]

48. Zheng, W.L.; Yang, W. Hydrothermal Synthesis of Diluted Magnetic Zn$_{1-x}$Mn$_x$O Semiconductor. *Appl. Mech. Mater.* **2013**, *313–314*, 184–187. [CrossRef]

49. Jain, K.; Pathak, S.; Kumar, P.; Singh, A.; Pant, R.P. Dynamic magneto-optical inversion in magnetic fluid using NanoMOKE. *J. Magn. Magn. Mater.* **2019**, *475*, 782–786. [CrossRef]

50. Kumar, P.; Pathak, S.; Jain, K.; Singh, A.; Basheed, G.A.; Pant, R.P. Low-temperature large-scale hydrothermal synthesis of optically active PEG-200 capped single domain MnFe$_2$O$_4$ nanoparticles. *J. Alloys Compd.* **2022**, *904*, 163992. [CrossRef]